


Pattern stabilization in swarms of programmable active matter: A probe for turbulence at large length scales

Pankaj Popli¹, Prasad Perlekar¹, and Surajit Sengupta^{*}

Tata Institute of Fundamental Research, Centre for Interdisciplinary Sciences, 36/P Gopanapally, Hyderabad 500046, India

 (Received 15 December 2020; accepted 1 September 2021; published 23 September 2021)

We propose an algorithm for creating stable, ordered, swarms of active robotic agents arranged in any given pattern. The strategy involves suppressing a class of fluctuations known as “nonaffine” displacements, *viz.*, those involving nonlinear deformations of a reference pattern, while all (or most) affine deformations are allowed. We show that this can be achieved using precisely calculated, fluctuating, thrust forces associated with a vanishing average power input. A surprising outcome of our study is that once the structure of the swarm is maintained at steady state, the statistics of the underlying flow field is determined solely from the statistics of the forces needed to stabilize the swarm.

DOI: [10.1103/PhysRevE.104.L032601](https://doi.org/10.1103/PhysRevE.104.L032601)

A bird flock or school of fish often shows large-scale collective and coordinated motion [1–8]. Such behavior not only protects individuals in the group from predators but also reduces hydrodynamic effects [8–12]. Pattern formation while flocking, of course, is an interplay between hydrodynamic interactions mediated by embedded fluid medium and how well swimmers respond to it [11–16]. Studies have shown that self-propelled agents, equipped with reinforcement learning algorithms, can adapt to minimize collective flying efforts and produce stable geometrical patterns [13]. Experiments have also used inanimate, autonomous agents such as active colloidal particles or robotic agents to mimic collective motion observed in nature [17–22].

The use of a patterned swarm of drones has shown immense potential in surveying, disaster management, and setting up a communication network in inaccessible locations [23–31]. Typical strategies for maintaining a pattern involves accurate measurement of the velocity of the fluid medium and actively compensating for the disruptive forces at the level of individual agents using computations performed at a central command and control station [32–34]. Although a fixed patterned arrangement of drones is obtained, the resulting swarm requires calm weather to operate and uses various collision avoidance and machine-learning algorithms, which increase operational and computational complexity [35–39].

In this letter, we propose a strategy to produce positionally ordered patterns of drones or robotic agents or “bots” [23,36,40] that are robust and do not require velocity sensors or any *a priori* knowledge of the underlying flow field. Another significant finding of our work is that in certain conditions, statistical properties of the underlying flow field can be obtained, as a coproduct, without using any invasive velocity probes. A common approach for studying flow statistics involves point particles that preferentially sample the flow structures or using an extended object such as a polymer if two-point correlations are needed [41–49]. In atmospheric

turbulence, these approaches are inefficient to obtain Eulerian statistics since particles separate quickly from one another due to turbulent diffusion [50]. This knowledge, on the other hand, would be of great help in interpreting wind patterns [51] and weather prediction [52], wind energy generation [53], understanding storms and hurricanes [54], etc.

Consider a system of bots placed in some pattern and embedded in a flowing medium. For specificity and computational simplicity, we consider here point particles placed at equal intervals in a circular geometry of radius R_s in two dimensions (see Fig. 1). Our analysis is general and unchanged if any other pattern or dimension is chosen. The particles have mass m and are allowed to move within a square box of length $L \gg R_s$. At any time t , the position \mathbf{r}_i and velocity \mathbf{v}_i of the i th particle is determined by the set of Stokes-drag equations [55] with a constant drag coefficient γ and in the presence of a background flow field $\mathbf{U}(\mathbf{r}_i, t)$, *viz.*,

$$\frac{d\mathbf{r}_i}{dt} = \mathbf{v}_i, \quad (1)$$

$$m \frac{d\mathbf{v}_i}{dt} = -\gamma[\mathbf{v}_i - \mathbf{U}(\mathbf{r}_i, t)] + \vec{\mathcal{F}}_i. \quad (2)$$

Here $\vec{\mathcal{F}}_i$ represents active forces produced by the bots’ own propulsion mechanism. These forces may, in principle, be programmed to mimic intrabot interactions arising from a virtual Hamiltonian. We put $m = 1$ for our subsequent analysis. Note that we assume that the bots are small in comparison to the typical flow structure so that their presence does not significantly alter the flow field $\mathbf{U}(\mathbf{r}_i, t)$.

Here $\mathbf{U}(\mathbf{r}, t)$ is the solution of the Navier-Stokes equations under appropriate boundary conditions and parameters representing fully developed turbulence. To reduce computational cost, however, we use a synthetic, multiscale, spatiotemporally correlated turbulent-like flow field as described in [56–58] for most of our results. We also show later that our main conclusions are unchanged if a realistic $\mathbf{U}(\mathbf{r}, t)$ obtained using direct numerical simulation (DNS) [59,60] is used.

^{*}Deceased.

The velocity of the field $\mathbf{U}(\mathbf{r}, t)$ at any given position and time is obtained from the Fourier series, $\mathbf{U}(\mathbf{r}, t) = V_0 \sum_{n=1}^{N_k} [\mathbf{A}_n \cos(\mathbf{k}_n \cdot \mathbf{r} + \omega_n t) + \mathbf{B}_n \sin(\mathbf{k}_n \cdot \mathbf{r} + \omega_n t)]$. Here N_k is the total number of Fourier modes included and V_0 is a dimensionless constant which determines the strength of the velocity field. Also, the Fourier coefficients \mathbf{A}_n , \mathbf{B}_n and distribution of modes \mathbf{k}_n , ω_n are chosen randomly with the constraint that the velocity field produced is incompressible and the energy spectrum follows Kolmogorov scaling $k^{-5/3}$; see the Supplemental Material (SM) [61].

What is the nature of the forces $\vec{\mathcal{F}}$ needed to maintain the shape of any given pattern (e.g., a ring) in the presence of turbulent field $\mathbf{U}(\mathbf{r}, t)$? It is easy to see that the simplest choice, *viz.*, nearest-neighbor harmonic forces [62–66], will not work. Local harmonic forces alone cannot guarantee the stability of the global pattern, and under the influence of a turbulent velocity field, the polymer quickly intertwines with itself and collapses [61]. Increasing the range of the harmonic forces is ineffective and simply increases the persistence length with intertwining happening further and further apart unless a large fraction of particles are bonded to each other [67]. This increases the computational and communication overheads for large swarms. An alternative may be to incorporate three-body forces that prefer particular bond angles [68,69]. Even in the presence of such interactions, the desired pattern may not be the unique ground state [70], and formulating such interactions may become cumbersome for more complex patterns. We describe below an algorithm which solves this problem, guaranteeing a unique global order using forces derived *only* from configurations of the local particle neighborhood.

We begin by observing that maintaining local particle connectivity guarantees global stability of any pattern, except for overall affine deformations, *i.e.*, all translations, rotations, dilations, and shears. The pattern is represented by a set of tagged (labeled) reference coordinates $\{\mathbf{R}_i\}$ for particles (bots) $i = 1, \dots, N$. Now, any set of particle displacements $\mathbf{u}_i = \mathbf{r}_i(t) - \mathbf{R}_i$ can be projected onto orthogonal nonaffine and affine subspaces [71,72] by a linear projection operator \mathbf{P} that we define shortly. The nonaffine part of the displacements involves particle rearrangements and changes the local connectivity of the neighborhood. We show that it is possible to determine time-dependent forces $\vec{\mathcal{F}}_i(t)$ that selectively suppress nonaffine displacements and therefore maintain local connectivity [73–76]. Since computation of $\vec{\mathcal{F}}_i(t)$ stems from a linear optimization problem, the desired reference structure is guaranteed to be the unique ground state [71,77]. While detailed discussions of the nonaffine projection formalism is given in [71,77] (see also SM [61]), we briefly recall the main ideas relevant to the present study.

Around each particle i , define a neighborhood $\Omega(i)$ consisting of the neighbors of the i th particle. In d dimension for a given coarse-graining volume consisting of $N_\Omega \leq N$ particles there exist d^2 affine and $N_\Omega d - d^2$ nonaffine displacement modes [71,77]. Clearly, for nonaffine displacement modes to exist, N_Ω requires to satisfy the obvious condition $N_\Omega > d$. For any generic deformation of $\Omega(i)$, we construct a block column vector Δ of size $N_\Omega d$ whose elements are $\Delta_{j\alpha} = u_j^\alpha - u_i^\alpha = (r_j^\alpha - r_i^\alpha) - (R_j^\alpha - R_i^\alpha)$, $\forall j \in \Omega(i)$, *i.e.*, the α th component of the relative displacement of particles i

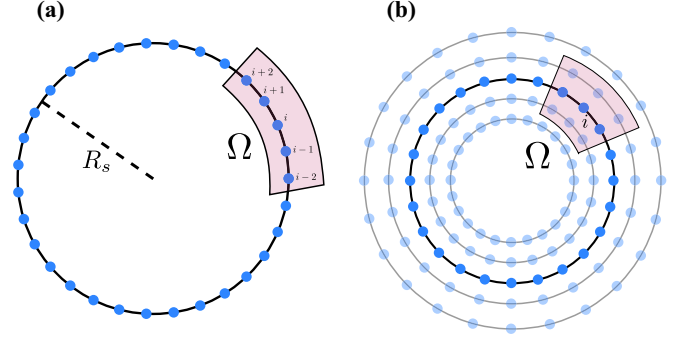


FIG. 1. Reference structure and coarse-graining volume Ω . (a) Model A: Floppy swarm, active particle spaced equally on a ring. Around particle i coarse-graining volume (pink shaded) is defined and consists of two left and right neighbors. (b) Model B: Rigid swarm, active particles equally spaced on a ring (dark blue) surrounded by layer of concentric ghost particles (light blue). Coarse-graining volume (pink shaded) around particle i consists of eight particles.

and j . Next we define the linear projection operator \mathbf{P} of Δ onto nonaffine subspace such that nonaffine component of displacements is given by $\mathbf{P}\Delta$ and $\chi_i(\{\mathbf{r}\}, \{\mathbf{R}\}) = \Delta^T \mathbf{P} \Delta$ measures total nonaffinity associated with the deformed $\Omega(i)$. The projection operator \mathbf{P} is a function only of the reference structure and is given by $\mathbf{P} = \mathbf{I} - \mathbf{M}(\mathbf{M}^T \mathbf{M})^{-1} \mathbf{M}^T$ with block matrix $M_{j\alpha, \mu\nu} = \delta_{\alpha\mu} (R_j^\nu - R_i^\nu)$, where R_j^ν, R_i^ν are ν th components of the desired reference position of active particles for $j \in \Omega(i)$ [61]. The active forces for the swarm are then defined as $\vec{\mathcal{F}}_i = -\partial(-h_X N X) / \partial \mathbf{r}_i$ where the parameter h_X determines the strength of nonaffine active forces conjugate to global nonaffinity field $X(\{\mathbf{r}\}, \{\mathbf{R}\}) = N^{-1} \sum_i \chi_i$. Note that although X is a multiparticle potential, it is fairly short-ranged, and only the neighboring drones within the coarse-grained region of a given bot indexed i contributes to the gradient of X (see Fig. 1 and SM [61] and Fig. S1). In other words, positional information of only the neighboring drones is required to calculate nonaffine forces, resulting in reduced communication and computational cost. By construction, negative values of h_X selectively suppress nonaffine displacements of the swarm while positive values enhance them. For any desired reference structure, the matrix \mathbf{P} is calculated and uploaded into the memory of drones. At any time t , a drone, i , can determine the forces $\vec{\mathcal{F}}_i(t)$ from the known instantaneous positions of its neighbors. Once applied in the form of extra thrust, these forces tend to reduce X and stabilize the pattern.

We introduce two distinct models, *viz.*, “Model A”: a *floppy* swarm and “Model B”: a *rigid* swarm; see Fig 1. In Model A we use a coarse-graining volume Ω consisting of four particles, *viz.*, two left and right neighbors of the central particle. On the other hand, in Model B, active particles are sandwiched between two concentric rings of “ghost” particles. The position of the particles in the ghost layers are not affected by the turbulent field or nonaffine forces and remain virtual, stored only in the memory of robotic agents. These virtual coordinates of ghost particles are free to translate and rotate along with particles of the actual swarm. The ghost

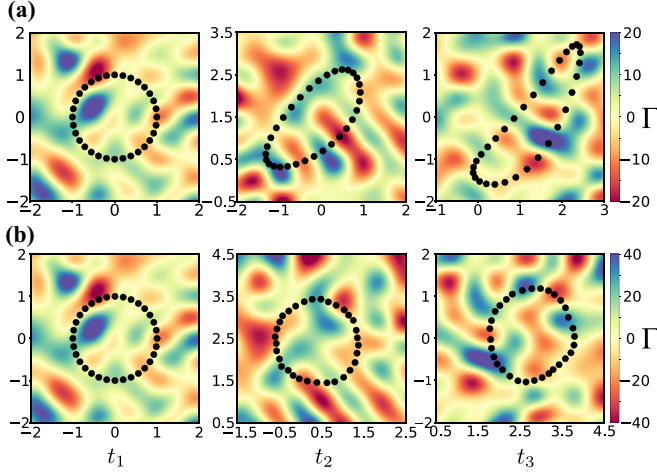


FIG. 2. Time evolution ($t_1 < t_2 < t_3$) of (a) Model A ($h_X = -1000, V_0 = 0.5$) and (b) Model B ($h_X = -1, V_0 = 1$) respectively. Background color represents the vorticity values ($\Gamma = \nabla \times \mathbf{U}$) of the turbulent field. In Model A, a global transformation of the circular ring to an ellipse is allowed and costs no energy. Model B, on the other hand, is stiffer. Only a portion of the full simulation cell has been shown for clarity.

particles in this setting satisfy rigid body constraints, and therefore their positions are updated by rigid translation and rotations, $\mathbf{r} + \mathbf{V}_{\text{com}}\delta t + \Phi\delta t\hat{z} \times (\mathbf{r} - \mathbf{R}_{\text{com}})$. Here $\mathbf{R}_{\text{com}}, \mathbf{V}_{\text{com}}$ and Φ are the center of mass position, velocity, and average angular velocity of the actual swarm. The ghost particle positions are included in the coarse-graining volume Ω and are taken into account while calculating \vec{F}_i for the actual bots. Coarse-graining volume for Model B thus consists of eight particles as shown in Fig. 1. Time-dependent configurations from Model A, shown in Fig. 2(a) reveal a stable elliptical pattern for sufficiently high values of h_X . For small h_X , while the ring may occasionally intertwine with itself, it is guaranteed to disentangle back, in sharp contrast to the harmonic case. Highly elliptical configurations are, however, observed. The transformation that takes a circle to an ellipse, and

and such deformations, no matter how much large, do not produce any nonaffinity in the system and are allowed as long as local neighborhood connectivity between particles is preserved. The presence of ghost particles in Model B serves as a “stencil” for the physical swarm, and all relative affine deformations of the swarm keeping ghost particles fixed are penalized. The only zero energy cost affine transformations are pure rotations and translations of the system as a whole. Figure 2(b) shows typical configurations of a Model B swarm.

It is clear that eddies with sizes much smaller than the size of the swarm cannot affect $\langle X \rangle$. On the other hand, very large eddies simply carry the swarm along introducing mainly affine deformations so that $\langle X \rangle \rightarrow 0$. Therefore $\langle X \rangle$ grows with decreasing eddy size saturating to a limit X_c for eddies below a cutoff size corresponding to frequency ω_c (see SM [61]). The only two dimensionless quantities are therefore $\langle X \rangle/X_c$ and $V_0^2\gamma\omega_c/|h_X|$ so that the leading behavior of $\langle X \rangle \sim V_0^2\gamma/|h_X|$ for both Models A and B as shown in Fig. 3. The greater flexibility of Model A implies power expended by nonaffine forces is much smaller compared to B as we discuss below.

Note that a constant $\langle X \rangle$ implies zero average power. Indeed, taking a dot product of both sides of the second equation in Eq. (2) with the velocity \mathbf{v}_i one obtains the rate of change of the kinetic energy ($= 0$ in the steady state) as $\vec{F}_i \cdot \mathbf{v}_i - \gamma(v_i^2 - \mathbf{U}(\mathbf{r}, t) \cdot \mathbf{v}_i)$. The first term is the power expended by the nonaffine forces and if \mathbf{v}_i follows the local fluid velocity $\mathbf{U}(\mathbf{r}, t)$; true for a swarm drifting along with the fluid medium, this is, on average zero. In practice, the distribution of power expended by \vec{F}_i fluctuates around zero with an error that is much smaller for Model A than for Model B as expected; see SM [61] for a detailed analysis for the specific case of the synthetic turbulent field used in this work.

We end this letter by demonstrating how the Model B swarm may be used to obtain the statistics of the turbulent flow field $\mathbf{U}(\mathbf{r}, t)$ over a few meters to kilometers. One may be able to measure the local velocity field using appropriate sensors and compute correlation functions and structure function “on the fly.” While this is of course possible, drone swarms, stabilized using forces which suppress X , can go a step further. Specifically, the swarm can be used to obtain equal-time

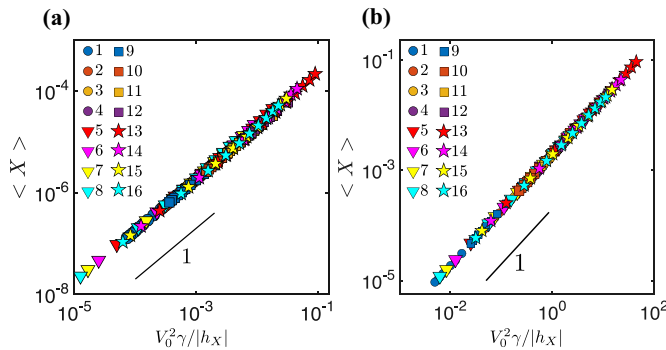


FIG. 3. Model A (a) and Model B (b): Global nonaffinity $\langle X \rangle$ scales linearly with $V_0^2\gamma/|h_X|$. Different symbols represents different combinations of the nonaffine field h_X, V_0 and γ (Stokes number). Since global nonaffinity measures the nonaffine deformation of the swarm, an increase in the value of X as a function of V_0 indicates the destabilizing tendency of the background flow. On the other hand, counteracting nonaffine forces tend to reduce these nonaffine deformations and therefore reduce X . A table of values of V_0, h_X , and γ for Models A and B used for generating (a) and (b) is also shown. The square brackets represent an interval with initial, final, and step values, respectively. The parentheses correspond to different value of γ .

S.No.	Model A		Model B		γ
	V_0	$-h_X$	V_0	$-h_X$	
1(9)	0.2	[100...550, 50]	0.1	[0.2...2, 0.2]	1(5)
2(10)	0.4	[100...550, 50]	0.3	[0.1...2, 0.2]	1(5)
3(11)	0.6	[100...550, 50]	0.5	[0.1...2, 0.2]	1(5)
4(12)	0.8	[100...550, 50]	0.7	[0.1...2, 0.2]	1(5)
5(13)	[0.1...1.9, 0.2]	200	[0.1...1.9, 0.2]	0.4	1(5)
6(14)	[0.1...1.9, 0.2]	400	[0.1...1.9, 0.2]	0.8	1(5)
7(15)	[0.1...1.9, 0.2]	600	[0.1...1.9, 0.2]	1.2	1(5)
8(16)	[0.1...1.9, 0.2]	800	[0.1...1.9, 0.2]	1.6	1(5)

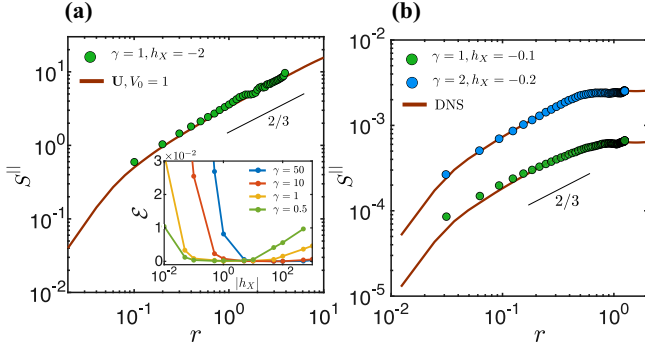


FIG. 4. Longitudinal structure function $S^{\parallel}(r)$ as a function of distance $r = |\mathbf{r}_{ij}|$ measured at Eulerian points (solid brown line) and using nonaffine forces (colored dots) in Model B. In (a) $\mathbf{U}(\mathbf{r}, t)$ is the same synthetic turbulent field used for earlier calculations. Simulation was done for a ring of radius $R_s = 2$, box size $L = 40$, and $N = 128$ particles. Inset shows linear regression error \mathcal{E} of the obtained nonaffine force structure function when compared to the expected $2/3$ law. Note that for a given value of γ , there exist a range of $|h_X|$ for which \mathcal{E} is minimum. (b) Same as in (a) but for $\mathbf{U}(\mathbf{r}, t)$ obtained from DNS with simulation parameters as $R_s = \pi/5$, box size $L = 2\pi$, and $N = 128$. To highlight the identical scaling, the velocity structure function obtained using the Eulerian flow field (solid brown line) is scaled by a constant prefactor.

measurements over a wide range of spatial length scales. This is useful to probe fields which involve flow structures at multiple length scales. To see this, we first point out that, interestingly, no knowledge of the velocity field is necessary to derive the active forces \vec{F}_i . They depend only on χ and therefore only on the knowledge of the instantaneous and reference positions of the neighbors. Obtaining information about positions is technically far easier than measuring local flow velocities. We calculate the longitudinal structure function [50] for nonaffine forces $S^{\parallel}_{\mathcal{F}}(r_{ij}) = \langle [(\vec{F}_i - \vec{F}_j) \cdot \hat{\mathbf{r}}_{ij}]^2 \rangle$ by binning equidistant pairs r_{ij} of drones and averaged over different realizations.

Figures 4(a) and 4(b) show the nonaffine force structure function together with the Eulerian form computed for our synthetic turbulent field $\mathbf{U}(\mathbf{r}, t)$ and the flow field obtained from DNS (see SM [61] for DNS details), respectively. The structure function of the nonaffine forces reproduces the Eulerian curve. The presence of ghost layers implies that all displacement of the bots except for uniform translation and rotations are considered nonaffine and are counterbalanced by the restoring nonaffine forces. Thus the swarm in Model B is analogous to elastic ring polymer [49] with the rigidity parameter as $|h_X|$. However, a key difference between a polymer and our swarm is that for zero or very small values of rigidity $|h_X|$, the swarm itself is not stable. The significance of $|h_X|$ on the stability of patterned swarm and

the structure function is motivated by [49] and is discussed below.

By looking at the momentum equation for the bots Eq. (2), it is possible to define two characteristic timescales, *viz.*, $\tau_\gamma = m/\gamma$ and $\tau_X = \sqrt{m/|h_X|}$, associated with the damping and swarm rigidity. Depending on the ratio of these timescales, various regimes of the swarm exist. For a given background field, the value of τ_γ is set by the mass and shape of the bots. For such a system the swarm itself is not stable for too small values of $|h_X|$, in contrast to the flexible polymer described in [49]. On the other hand, a large value of rigidity ($|h_X|$) pushes normal modes of the swarm towards the higher frequencies with either little or no overlap with the frequency spectra of the turbulent field. Drawing analogy to a driven oscillator, the amplitude corresponding to driving frequencies (turbulent frequencies) becomes significantly small such that any fluctuations created by the background field dampen quickly with timescale τ_X . The deformation of the swarm is therefore not subject to turbulence. This immediately suggests an optimum value of $|h_X|$ for which nonaffine forces are proportional to the background velocity field and yields the desired structure function. To identify the optimum value of $|h_X|$, we plot (Fig. 4 inset) the linear regression error $\mathcal{E} = \langle [1 - S^{\parallel}_{\mathcal{F}}(r)r^{-2/3} / \langle S^{\parallel}_{\mathcal{F}}(r)r^{-2/3} \rangle_r]^2 \rangle_r$ of the nonaffine force structure function obtained compared to the predicted $2/3$ law for various values of γ and $|h_X|$. The inset of Fig. 4(b) clearly shows a range of the optimum value of $|h_X|$ for which \mathcal{E} is the minimum and the structure function of the nonaffine forces yields the predicted $2/3$ behavior. Therefore, an imprint of the statistics of $\mathbf{U}(\mathbf{r}, t)$ is present in the statistics of the nonaffine forces used to stabilize the swarm! Note that large values of γ also require large values of $|h_X|$ to stabilize. While, of course, this is achievable in simulations, in the real world it is limited by the aerodynamics, design, and capacity of the drones to produce the required thrust.

This surprising result elucidates a very important aspect of the Model B swarm. Since nonaffine forces need to be computed anyway in order to stabilize the structure, no extra measurements are required for obtaining the structure function of the background flow field. The set of robotic agents such as drones can be set up as a Model B swarm to probe the statistics of the atmospheric turbulence at large length scales. It is also easy to make a swarm switch between Model A and Model B modes because the difference is only in the reference configurations. The swarm can, therefore, fly in the floppy mode to conserve energy but switch to a stiffer configuration when a measurement of $S^{\parallel}(r_{ij})$ is needed.

We thank S. Ganguly, P. Nath, K. Ramola, V. Pandey, and N. Rana for useful discussions. Intramural support at TIFR Hyderabad from Department of Atomic Energy, Government of India, is gratefully acknowledged. P. Popli and P. Perlekar acknowledge the contributions of Surajit Sengupta, now sadly deceased, to the development and completion of this work.

[1] A. Cavagna and I. Giardinà, *Annu. Rev. Condens. Matter Phys.* **5**, 183 (2014).

[2] H. Hildenbrandt, C. Carere, and C. K. Hemelrijk, *Behav. Ecol.* **21**, 1349 (2010).

- [3] W. F. Loomis, *The Development of Dictyostelium Discoideum* (Academic, New York, 1982).
- [4] W. J. Rappel, A. Nicol, A. Sarkissian, H. Levine, and W. F. Loomis, *Phys. Rev. Lett.* **83**, 1247 (1999).
- [5] K. B. Raper, S. M. Pady, P. L. Lentz, Robert W. Lichtwardt, C. M. Wetmore, J. A. Stevenson, L. R. Batra, M. S. Fuller, and R. P. Korf, *Mycologia* **60**, 211 (1968).
- [6] C. W. Reynolds, in *Proceedings of the 14th Annual Conference on Computer Graphics and Interactive Techniques (SIGGRAPH '87)* (Association for Computing Machinery, New York, NY, USA, 1987), pp. 25–34.
- [7] A. Huth and C. Wissel, The movement of fish schools: A simulation model, in *Biological Motion*, edited by W. Alt and G. Hoffmann, Lecture Notes in Biomathematics Vol. 89 (Springer, Berlin, Heidelberg, 1990), pp. 577–595.
- [8] B. L. Partridge, *Sci. Am.* **246**, 114 (1982).
- [9] P. F. Major, *Anim. Behav.* **26**, 760 (1978).
- [10] L. Landeau and J. Terborgh, *Anim. Behav.* **34**, 1372 (1986).
- [11] Y. Hatwalne, S. Ramaswamy, M. Rao, and R. A. Simha, *Phys. Rev. Lett.* **92**, 118101 (2004).
- [12] R. A. Simha and S. Ramaswamy, *Phys. Rev. Lett.* **89**, 058101 (2002).
- [13] M. Gazzola, A. A. Tchieu, D. Alexeev, A. De Brauer, and P. Koumoutsakos, *J. Fluid Mech.* **789**, 726 (2016).
- [14] A. Gupta, A. Roy, A. Saha, and S. S. Ray, *Phys. Rev. Fluids* **5**, 052601(R) (2020).
- [15] R. A. Simha and S. Ramaswamy, *Physica A* **306**, 262 (2002).
- [16] J. Toner, *Phys. Rev. Lett.* **108**, 088102 (2012).
- [17] A. Bricard, J. B. Caussin, N. Desreumaux, O. Dauchot, and D. Bartolo, *Nature (London)* **503**, 95 (2013).
- [18] D. Geyer, A. Morin, and D. Bartolo, *Nat. Mater.* **17**, 789 (2018).
- [19] H. Levine, W. J. Rappel, and I. Cohen, *Phys. Rev. E* **63**, 041510 (2001).
- [20] G. Wang, T. V. Phan, S. Li, M. Wombacher, J. Qu, Y. Peng, G. Chen, D. I. Goldman, S. A. Levin, R. H. Austin, and L. Liu, *Phys. Rev. Lett.* **126**, 108002 (2021).
- [21] T. Vicsek, A. Czirok, E. Ben-Jacob, I. Cohen, and O. Shochet, *Phys. Rev. Lett.* **75**, 1226 (1995).
- [22] A. Czirok, H. E. Stanley, and T. Vicsek, *J. Phys. A: Math. Gen.* **30**, 1375 (1997).
- [23] D. Floreano and R. J. Wood, *Nature* **521**, 460 (2015).
- [24] A. L. Alfeo, M. G. Cimino, N. De Francesco, M. Lega, and G. Vaglini, *J. Comput. Sci.* **29**, 19 (2018).
- [25] P. Tosato, D. Facinelli, M. Prada, L. Gemma, M. Rossi, and D. Brunelli, in *20th IEEE International Symposium on A World of Wireless, Mobile and Multimedia Networks, WoWMoM 2019* (Institute of Electrical and Electronics Engineers, 2019).
- [26] J. Ahmad, Broadband access system via drone/UAV platforms, U.S. Patent 9853715, Dec. 2017.
- [27] M. Mozaffari, W. Saad, M. Bennis, Y. H. Nam, and M. Debbah, *IEEE Commun. Surv. Tutor.* **21**, 2334 (2019).
- [28] M. A. Khan, I. M. Qureshi, and F. Khanzada, *Drones* **3**, 16 (2019).
- [29] Google X, Project Loon, <http://www.x.company/loon/>.
- [30] Space X, Project Starlink, <https://www.starlink.com>.
- [31] IBM, Project Owl, <https://developer.ibm.com/callforcode/solutions/owl/>, <https://www.project-owl.com/about>.
- [32] S. Sinha, R. Ramaswamy, and J. S. Rao, *Physica D* **43**, 118 (1990).
- [33] S. Sinha, *Phys. Lett. A* **156**, 475 (1991).
- [34] F. Golnaraghi and B. C. Kuo, *Automatic Control Systems*, Tenth Edition (McGraw-Hill Education, New York, Chicago, 2017), p. 609.
- [35] A. Majid, A. Ashraf, E. Troubitsyna, and M. Daneshtalab, in *Proceedings—26th Euromicro International Conference on Parallel, Distributed, and Network-Based Processing, PDP 2018* (Institute of Electrical and Electronics Engineers, 2018), pp. 101–108.
- [36] Intel, Drone light shows powered by Intel, <https://www.intel.in/content/www/in/en/technology-innovation/aerial-technology-light-show.html> and <https://inteldronelightshows.com/performance/xxiii-olympic-winter-games/>.
- [37] N. Khurana and N. T. Ouellette, *New J. Phys.* **15**, 095015 (2013).
- [38] G. Vásárhelyi, C. Virág, G. Somorjai, T. Nepusz, A. E. Eiben, and T. Vicsek, *Sci. Robot.* **3**, eaat3536 (2018).
- [39] A. Choudhary, D. Venkataraman, and S. Sankar Ray, *Europhys. Lett.* **112**, 24005 (2015).
- [40] G. H. Elkaim, F. A. Pradipta Lie, and D. Gebre-Egziabher, in *Handbook of Unmanned Aerial Vehicles*, edited by K. Valavanis and George J. Vachtsevanos (Springer Netherlands, 2015).
- [41] L. Ducasse and A. Pumir, *Phys. Rev. E* **77**, 066304 (2008).
- [42] M. M. Bandi, J. R. Cressman, and W. I. Goldberg, *J. Stat. Phys.* **130**, 27 (2008).
- [43] C. C. Lalescu and M. Wilczek, *New J. Phys.* **20**, 13001 (2018).
- [44] R. Singh, M. Gupta, J. R. Picardo, D. Vincenzi, and S. S. Ray, *Phys. Rev. E* **101**, 053105 (2020).
- [45] J. R. Picardo, D. Vincenzi, N. Pal, and S. S. Ray, *Phys. Rev. Lett.* **121**, 244501 (2018).
- [46] A. Ali, E. L. C. V. M. Plan, S. S. Ray, and D. Vincenzi, *Phys. Rev. Fluids* **1**, 082402(R) (2016).
- [47] J. Bec, *Phys. Fluids* **15**, L81 (2003).
- [48] K. Gustavsson and B. Mehlig, *Adv. Phys.* **65**, 1 (2016).
- [49] M. E. Rosti, A. A. Banaei, L. Brandt, and A. Mazzino, *Phys. Rev. Lett.* **121**, 044501 (2018).
- [50] U. Frisch, *Turbulence* (Cambridge University Press, 1995).
- [51] C. Wang, Z. Lu, and Y. Qiao, Modeling of wind pattern and its application in wind speed forecasting, in *2009 International Conference on Sustainable Power Generation and Supply* (IEEE, Piscataway, NJ, 2009).
- [52] L. F. Richardson, *Weather Prediction by Numerical Process*, 2nd ed. (Cambridge University Press, Cambridge, 1922), p. 231.
- [53] M. M. Bandi, *Phys. Rev. Lett.* **118**, 028301 (2017).
- [54] Scientists hope to steer robotic surfboards into hurricanes, Matthew Cappucci, The Washington Post, June 1, 2021, <https://www.washingtonpost.com/weather/2021/06/01/surfboard-saildrone-hurricanes/>.
- [55] G. K. Batchelor, *An Introduction to Fluid Dynamics* (Cambridge University Press, 2000).
- [56] J. C. H. Fung and J. C. Vassilicos, *Phys. Rev. E* **57**, 1677 (1998).
- [57] J. C. Fung, J. C. Hunt, N. A. Malik, and R. J. Perkins, *J. Fluid Mech.* **236**, 281 (1992).
- [58] F. Nicolleau and G. Yu, *Phys. Fluids* **16**, 2309 (2004).
- [59] P. Perlekar, N. Pal, and R. Pandit, *Sci. Rep.* **7**, 44589 (2017).
- [60] Z. Xiao, M. Wan, S. Chen, and G. L. Eyink, *J. Fluid Mech.* **619**, 1 (2009).

- [61] See Supplemental Material at <http://link.aps.org/supplemental/10.1103/PhysRevE.104.L032601> for more details, which also includes Refs. [78–80].
- [62] C. Brouzet, G. Verhille, and P. Le Gal, *Phys. Rev. Lett.* **112**, 074501 (2014).
- [63] G. Verhille and A. Bartoli, *Exp. Fluids* **57**, 117 (2016).
- [64] A. Gay, B. Favier, and G. Verhille, *Europhys. Lett.* **123**, 24001 (2018).
- [65] D. Dotto and C. Marchioli, *Acta Mech.* **230**, 597 (2019).
- [66] S. Allende, C. Henry, and J. Bec, *Phys. Rev. Lett.* **121**, 154501 (2018).
- [67] J. C. Maxwell, *London Edinburgh Dublin Philos. Mag. J. Sci.* **27**, 294 (1864).
- [68] P. N. Keating, *Phys. Rev.* **145**, 637 (1966).
- [69] J. G. Kirkwood, *J. Chem. Phys.* **7**, 506 (1939).
- [70] H. Kedia, D. Pan, J.-J. Slotine, and J. L. England, [arXiv:1908.09332](https://arxiv.org/abs/1908.09332) (2019).
- [71] S. Ganguly, S. Sengupta, P. Sollich, and M. Rao, *Phys. Rev. E* **87**, 042801 (2013).
- [72] S. Ganguly, S. Sengupta, and P. Sollich, *Soft Matter* **11**, 4517 (2015).
- [73] P. Popli, S. Ganguly, and S. Sengupta, *Soft Matter* **14**, 104 (2017).
- [74] S. Ganguly, P. Nath, J. Horbach, P. Sollich, S. Karmakar, and S. Sengupta, *J. Chem. Phys.* **146**, 124501 (2017).
- [75] S. Ganguly, D. Das, J. Horbach, P. Sollich, S. Karmakar, and S. Sengupta, *J. Chem. Phys.* **149**, 184503 (2018).
- [76] A. Mitra, S. Ganguly, S. Sengupta, and P. Sollich, *J. Stat. Mech.: Theory Exp.* (2015) P06025.
- [77] P. Popli, S. Kayal, P. Sollich, and S. Sengupta, *Phys. Rev. E* **100**, 033002 (2019).
- [78] N. Grønbech-Jensen and O. Farago, *Mol. Phys.* **111**, 983 (2013).
- [79] V. S. Reddy, P. Nath, J. Horbach, P. Sollich, and S. Sengupta, *Phys. Rev. Lett.* **124**, 025503 (2020).
- [80] P. Nath, S. Ganguly, J. Horbach, P. Sollich, S. Karmakar, and S. Sengupta, *Proc. Nat. Acad. Sci. USA* **115**, E4322 (2018).